

A SPACE-BASED OBSERVATIONAL STRATEGY FOR CHARACTERIZING THE FIRST STARS AND GALAXIES USING THE REDSHIFTED 21-CM GLOBAL SPECTRUM

JACK O. BURNS¹, RICHARD BRADLEY⁶, KEITH TAUSCHER^{1,2}, STEVEN FURLANETTO³, JORDAN MIROCHA³, RAUL MONSALVE^{1,5}, DAVID RAPETTI^{1,9}, WILLIAM PURCELL¹³, DAVID NEWELL¹³, DAVID DRAPER¹³, ROBERT MACDOWALL⁴, JUDD BOWMAN⁵, BANG NHAN^{1,6}, EDWARD J. WOLLACK⁴, ANASTASIA FIALKOV⁸, DAYTON JONES¹¹, JUSTIN C. KASPER⁷, ABRAHAM LOEB⁸, ABHIRUP DATTA^{1,12}, JONATHAN PRITCHARD¹⁰, ERIC SWITZER⁴, MICHAEL BICAY⁹,¹Center for Astrophysics and Space Astronomy, Department of Astrophysical and Planetary Science, University of Colorado, Boulder, CO 80309, USA²Department of Physics, University of Colorado, Boulder, CO 80309, USA³Department of Physics and Astronomy, University of California at Los Angeles, Los Angeles, CA 90095, USA⁴NASA Goddard Space Flight Center, Greenbelt, MD 20771, USA⁵Arizona State University, School of Earth and Space Exploration, P.O. Box 876004, Tempe, AZ 85287, USA⁶National Radio Astronomy Observatory, 520 Edgement Road, Charlottesville, VA 22903, USA⁷Department of Climate and Space Sciences and Engineering, University of Michigan, Ann Arbor, MI 48109, USA⁸Center for Astrophysics, 60 Garden St., MS 51, Cambridge, MA 02138, USA⁹NASA Ames Research Center, Moffett Field, CA 94035, USA¹⁰Department of Physics, Blackett Laboratory, Imperial College, London SW7 2AZ, UK¹¹Space Science Institute, 4750 Walnut Street, Suite 205, Boulder, CO 80301, USA¹²Indian Institute of Technology, Indore, India and¹³Ball Aerospace Corporation, 1600 Commerce Street, Boulder, CO 80301 USA

Draft version January 13, 2022

ABSTRACT

The redshifted 21-cm monopole is expected to be a powerful probe of the epoch of the first stars and galaxies ($10 < z < 35$). The global 21-cm signal is sensitive to the thermal and ionization state of hydrogen gas and thus provides a tracer of sources of energetic photons – primarily hot stars and accreting black holes – which ionize and heat the high redshift intergalactic medium (IGM). This paper presents a strategy for observations of the global spectrum with a realizable instrument placed in a low altitude lunar orbit, performing night-time 40-120 MHz spectral observations, while on the farside to avoid terrestrial radio frequency interference, ionospheric corruption, and solar radio emissions. The frequency structure, uniformity over large scales, and unpolarized state of the redshifted 21-cm spectrum are distinct from the spectrally featureless, spatially-varying, and polarized emission from the bright foregrounds. This allows a clean separation between the primordial signal and foregrounds. For signal extraction, we model the foreground, instrument, and 21-cm spectrum with eigenmodes calculated via Singular Value Decomposition analyses. Using a Markov Chain Monte Carlo algorithm to explore the parameter space defined by the coefficients associated with these modes, we illustrate how the spectrum can be measured and how astrophysical parameters (e.g. IGM properties, first star characteristics) can be constrained in the presence of foregrounds using the *Dark Ages Radio Explorer* (DARE).

Keywords: cosmology: dark ages, reionization, first stars - cosmology: observations

1. INTRODUCTION

One of the last frontiers of observational cosmology is the time period stretching from the end of the Dark Ages through Cosmic Dawn (≈ 80 –500 million years after the Big Bang). This is a virtually unobserved yet key epoch in the early Universe. During this interval, the first luminous objects including stars, galaxies, and accreting black holes “turned on” (e.g., [Loeb & Furlanetto 2013](#)). Furthermore, this time period saw the birth of structural complexity in the Universe. At the beginning of the Dark Ages, corresponding to the Epoch of Recombination, the Universe was smooth to 1 part in 10^5 as evidenced by the Cosmic Microwave Background (CMB; e.g., [Mather et al. 2013](#)). Yet less than a billion years later, the Universe was teeming with complex structure. Thus, this transition time in the Universe is vital to understanding how the core components and structures of today’s Universe came to be.

The highly-redshifted 21-cm spectral line of neutral hydrogen, produced by a spin-flip hyperfine transition ([Ewen & Purcell 1951](#); [Field 1958](#)), provides an ob-

servable window into the early Universe’s intergalactic medium (IGM) before the Epoch of Reionization (EoR) was complete ([Madau et al. 1997a](#)). The heating and ionization caused by the “first objects to light up the Universe”¹ serve as indirect probes of the nature of the first stars and galaxies. With an effective optical depth of $\approx 1\%$ and sensitivity to low temperatures, the resulting signal measured against the CMB permits us to investigate a large evolutionary range from the Dark Ages through the end of the EoR (e.g., [Furlanetto et al. 2006](#); [Morales & Wyithe 2010](#); [Pritchard & Loeb 2012](#)).

The 21-cm all-sky or global signal ([Shaver et al. 1999](#); [Pritchard & Loeb 2010](#)) (Figure 1) is an attractive observational target for either a single antenna (e.g., [Bowman & Rogers 2010](#); [Burns et al. 2012](#); [Patra et al. 2013](#); [Voytek et al. 2014](#); [Bernardi et al. 2015](#); [Sokolowski et al. 2015a](#)) or a small, compact array of antennas (e.g., [Presley et al. 2015](#); [Vedantham et al. 2015](#); [Singh et al. 2015](#)). Features in the spectrum may provide the first

¹ NRC Astrophysics Decadal Survey: New Worlds, New Horizons in Astronomy and Astrophysics, <http://www.nap.edu/catalog/12951/new-worlds-new-horizons-in-astronomy-and-astrophysics>.

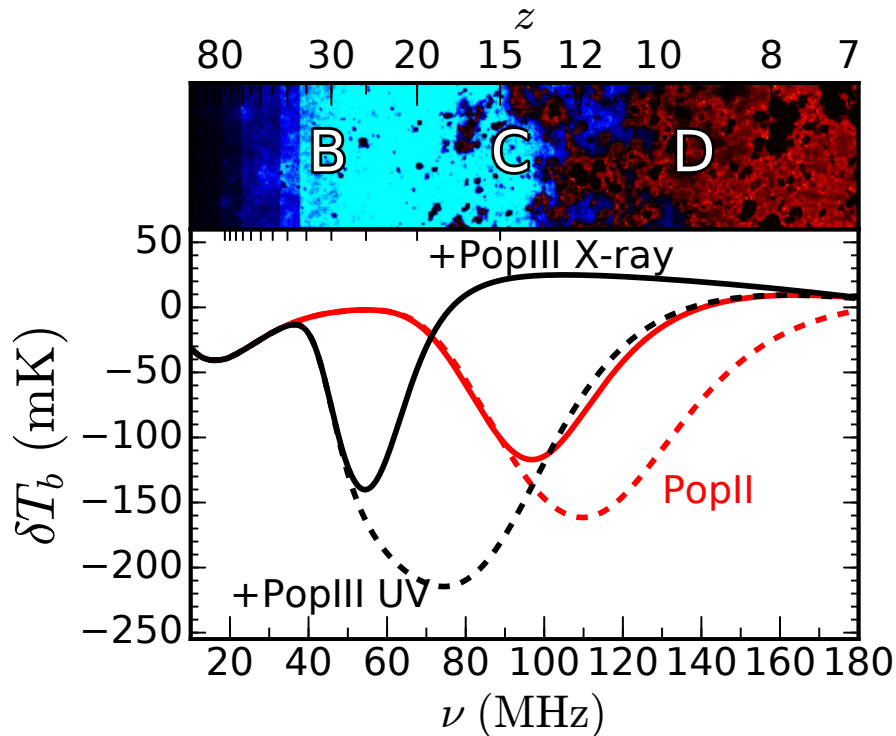


Figure 1. Evolution of a slice of the Universe, from early times (left, upper panel) to late times (right) as well as several different models for the corresponding 21-cm spectrum relative to the CMB (lower panel). The red lines are conservative estimates with Pop II (metal-rich) stars only, while the black curves assume that Pop III (metal-free) star formation also occurs, but only in low-mass galaxies where atomic cooling is inefficient. The dashed and solid black curves assume that Pop III stars are distinct from Pop II stars in their emission properties – 100 times brighter in the UV (dashed) and in the UV + X-ray emissions (solid), respectively. The dashed red curve assumes stellar properties corresponding to low redshift Pop II stars whereas the solid red curve corresponds to metallicities of 5% solar. Designations B, C and D indicate the redshift corresponding to the ignition of first stars, the formation of initial black hole accretion, and the onset of reionization, respectively. See Section 6 for further discussion. Figure adapted from Pritchard & Loeb (2010) using the new reference models from Mirocha et al. (2017).

constraints on the birth and nature of the first luminous objects (e.g., Furlanetto 2006). Such an experiment for 21-cm cosmology is analogous to the COBE measurement of the CMB blackbody spectrum, which set the stage for more detailed studies of spatial fluctuations by WMAP and Planck.

In this paper, we describe a space-based strategy for observations of the 21-cm global signal that probes the time of formation and the characteristics of the first stars and galaxies. We demonstrate how signal extraction using a realizable radiometer system and Bayesian statistical techniques, in the presence of strong galactic and extragalactic foregrounds, can measure spectral features and constrain the physical properties of the first luminous objects. We use the new detailed design of the *Dark Ages Radio Explorer* (DARE) to illustrate how the 21-cm spectrum can be extracted from the foreground using a feasible observational strategy.

DARE is proposed to conduct observations between 40 and 120 MHz in an orbit around the Moon with data taken only above the lunar farside. On Earth, the ionosphere corrupts low frequency observations (see e.g., Vedantham et al. 2014; Vedantham & Koopmans 2015; Rogers et al. 2015; Sokolowski et al. 2015b; Datta et al. 2016 and references therein) due to refraction, absorp-

tion, and emission driven by solar emissions and the solar wind (Davies 1990; Liu et al. 2011; Polygiannakis et al. 2003). At 50 km above the lunar farside, >90 dB of radio frequency interference (RFI) attenuation produces an environment quiet to <1 mK (e.g., McKinley et al. 2013). In addition, the Moon shields the instrument (about half the time) from variable solar emission caused by flares and coronal activity (e.g., Mercier & Trotter 1997). Therefore, observations above the nighttime, pristine, radio-quiet lunar farside (as verified by RAE-2, Alexander & Kaiser 1976) bypass the challenges presented by the Earth and the Sun and provide an optimal site for measurements of the global 21-cm signal.

The key insight permitting the Cosmic Dawn signal to be detected in the presence of bright foregrounds is that once the Moon blocks solar effects and terrestrial RFI, the foregrounds are significantly different in their characteristics from the expected 21-cm spectral signal. The 21-cm monopole strength is about four orders of magnitude weaker than the Galactic foreground. However, the 21-cm signal is separable from the foreground because it is spatially uniform at angular scales $\gtrsim 10^\circ$ (e.g., Bittner & Loeb 2011; Liu et al. 2013), unpolarized, and has distinct spectral features whereas the observed foreground varies spatially, exhibits polarized emission,

and is spectrally featureless. The 21-cm cosmological signal can then be extracted using algorithms similar to those employed for CMB observations implemented via a Markov Chain Monte Carlo framework (Harker et al. 2012, 2016).

The paper is organized as follows. In Section 2, we introduce and summarize the space-based observational strategy. In Section 3, an overview of the stellar models for the sky-averaged 21-cm signal used to develop the observational strategy is presented. Section 4 describes the nature and brightness of astronomical foregrounds which must be considered in efforts to measure the much weaker Cosmic Dawn signal. Section 5 provides a synopsis of the new design for DARE. Section 6 describes our software pipeline for signal extraction. In Section 7, we discuss the physical parameters (and their uncertainties) associated with the first stars, black holes, and galaxies that are expected to be measured using the 21-cm all-sky spectrum. Section 8 presents a summary of the potential use of the 21-cm background to detect the first luminous objects in the early Universe.

2. SUMMARY OF THE OBSERVATIONAL STRATEGY

Here we briefly describe key aspects of our observational strategy. The following sections will provide details about each item, as well as their relevance to the overall tactic. The core components of the strategy are as follows:

- We incorporate a wide range of theoretical models ($> 1.5 \times 10^4$) from two different classes of possible signals, differing by the generation of stars whose contribution dominates the behavior of the signal (Pop II or Pop III). We show that the DARE instrument in orbit of the Moon can effectively differentiate between these models using our Bayesian inference pipeline.
- We realistically model the diffuse foregrounds accounting for spatial variations of their spectral index, which is estimated from all-sky, publicly available maps at two frequencies (45 and 408 MHz).
- The new DARE reference instrument design incorporates (1) an optimized antenna with on-orbit beam calibration, (2) the replacement of Dicke switches for bandpass calibration with a pilot frequency tone system capable of high dynamic range monitoring of gain variations and measurements of the system reflection coefficients, and (3) polarimetric observations to provide a model-independent measure of the beam-averaged foregrounds. The observations, performed from the radio-quiet zone above the Moon’s farside, will be enabled through a unique “frozen” 50×125 km lunar equatorial orbit (Plice et al. 2017). The nominal observation time corresponds to 800 hours, which results in radiometric noise integration to the 1.7 mK level at 60 MHz. The instrument provides data with the frequency range (40 – 120 MHz), spectral resolution (50 kHz), beam characteristics ($\approx 60^\circ$ FWHM at 60 MHz), and polarization required to measure the spectral features expected

from the wide range of theoretical models considered. DARE’s present-day observing strategy utilizes four quiet-sky pointing directions away from the galactic center.

- Our signal extraction pipeline is centered around a Singular Value Decomposition (SVD) approach, which allows us to robustly separate the 21-cm signal from the additional contributions to the measurement by using orthogonal modes of variation of each component. These modes are determined from well-characterized training sets constructed from either theory or measurements.

We constructed a detailed end-to-end observation model that generates simulated antenna temperatures using our models for the diffuse foregrounds and the 21-cm spectrum, and the predicted telescope pointing, Moon location, and instrument characteristics. Unlike previous papers (e.g., Mirocha et al. 2015; Harker et al. 2016), which assumed perfect knowledge of the instrument, this new process accounts for and propagates the uncertainty in the instrumental parameters to the signal extraction pipeline. Our instrument sensitivity metric is defined as the RMS uncertainty of the extracted 21-cm spectrum, averaged over the observation band. Our requirement for this metric is to keep it below 20 mK for all models processed with our pipeline.

3. MODELS FOR THE 21-CM GLOBAL SIGNAL

In this section we discuss the global 21 cm signal, and describe the broad set of physical models that are incorporated into our analysis strategy.

The 21-cm global signal arises from the radiation effects produced by the first stars, accreting black holes, and galaxies on the surrounding IGM. X-ray and UV emission from these objects and their descendants heated and ionized the tenuous gas that lies between galaxies, culminating in the Epoch of Reionization several hundred Myrs later. The 21-cm background can be used to measure these radiation effects with the hyperfine line of the neutral hydrogen (HI) gas pervading the Universe. The expansion of the Universe redshifts these photons from earlier epochs to lower observed frequencies, $\nu = 1420/(1+z)$ MHz (e.g., at $z = 30$, $\nu = 45$ MHz). Importantly, this frequency-redshift relation enables a direct reconstruction of the history of the Universe as a function of time from the 21-cm spectrum.

Figure 1 shows some example predictions (amongst those currently allowed) for the 21-cm spectrum during the Dark Ages and Cosmic Dawn. The brightness temperature of this 21-cm signal is given by (e.g., Madau et al. 1997b; Shaver et al. 1999; Furlanetto et al. 2006)

$$\delta T_b \simeq 27 x_{\text{HI}} \left(\frac{T_s - T_{\text{CMB}}}{T_s} \right) \left(\frac{1+z}{10} \right)^{1/2} (1 + \delta_B) \left[\frac{\partial_r v_r}{(1+z)H(z)} \right]^{-1} \text{ mK}, \quad (1)$$

where x_{HI} is the fraction of neutral gas, T_s is the 21-cm spin temperature, T_{CMB} is the CMB temperature, δ_B is the baryon overdensity (taken here to be $\delta_B \sim 0$), and $H(z)$ is the Hubble parameter. The last term in

this equation includes the effect of the peculiar velocities with line of sight velocity derivative $\partial_r v_r$. Since we will measure the spatially averaged δT_b , the effects of the last term in Equation 1 are negligible for observations of the 21-cm global signal (e.g., Bharadwaj & Ali 2004; Barkana & Loeb 2005).

Several important physical processes drive the evolution of δT_b with redshift. These include: (1) UV radiation from the first stars, which “activates” the spin-flip signal through the Wouthuysen-Field mechanism (Wouthuysen 1952; Field 1958); (2) X-ray heating, likely generated by gas accretion onto the first black holes; and (3) ionizing photons from the first galaxies (which destroy the neutral hydrogen).

The relevant radiation backgrounds grow at different times, so their interplay creates distinct features in the spectrum (Furlanetto et al. 2006; Pritchard & Loeb 2010; Mesinger et al. 2011). When the first stars appear, their UV radiation drives T_s toward the cold temperatures that are characteristic of IGM gas ($z \sim 35 - 22$ across our range of models; Region B in Figure 1), triggering a deep absorption trough (Madau et al. 1997a). Shortly after, black holes likely formed, e.g., as remnants of the first stars ($z \sim 25 - 12$ across our range of models; Region C). The energetic X-ray photons from these accreting black holes travel great distances, eventually ionize H and He atoms, and produce photo-electrons that deposit some of their energy as heat in the IGM (Shull & van Steenberg 1985; Furlanetto & Johnson Stoeve 2010), transforming the 21-cm signal from absorption into emission as the gas becomes hotter than the CMB (Region D). The emission peaks as photons from these stars and black holes ionize the IGM gas ($z < 12$), eventually eliminating the spin-flip signal.

The dashed red curve in Figure 1 assumes that the efficiency and properties of star formation in early galaxy populations (Sun & Furlanetto 2016; Mirocha et al. 2017) and the relationship between X-ray luminosity and star formation rate are the same as at later times (Mineo et al. 2012b). There are several reasons to expect that this Pop II model is conservative, i.e., that it underestimates the total production rate of UV and X-ray photons. For example, it assumes solar metallicity, though stars in high- z galaxies are likely forming in metal-poor environments, which can boost their UV (Eldridge & Stanway 2009) and X-ray outputs (Brorby et al. 2016). The solid red curve in Figure 1 assumes that galaxies have metallicities (Z) 5% of solar, which results in a shallower absorption feature due to enhanced X-ray emission (assuming the Brorby et al. 2016 L_X -SFR- Z relation). Alternatively, the black curves include a simple model for Pop III stars, in which low-mass halos (below atomic cooling threshold) can produce UV and X-ray photons (neglected by red curves). Boosts of 100 in the efficiency of the UV (dashed black) and also the X-ray luminosity (solid black) of Pop III stars relative to Pop II result in a variety of qualitatively different predictions for the global 21-cm signal. Pop III models that resemble our black curves should be relatively straightforward to distinguish from Pop II-only models for an experiment like DARE (see Section 6 and Figure 7). At this stage, our ability to label each set of curves as being Pop II- or Pop III-dominated assumes that the current Pop II models are well calibrated (Mirocha et al. 2017). New measurements

(by e.g., JWST) in the coming years can be immediately incorporated into the model, and will act to mitigate degeneracies between Pop II and Pop III sources. More subtle features of the signal, such as its asymmetry, may also reveal the presence of Pop III despite uncertainties in the calibration of Pop II models (Mirocha et al., in preparation).

It is also worth noting that the 21-cm global signal traces the collective effects of all sources in the redshift ranges illustrated in Figure 1, which form a mostly unresolved sea of fainter objects that likely dominate the total emissivity of the early Universe. The red curves in Figure 1 are calibrated to match the latest luminosity function measurements from HST (which probe relatively bright galaxies that can be resolved) and CMB optical depth (τ_e) measurements from Planck (Mirocha et al. 2017), with variations arising solely due to differences in the adopted properties of galaxies beyond the current detection threshold. JWST and future CMB missions will further constrain the bright-end of the galaxy luminosity function and τ_e , respectively, and will thus enhance the sensitivity of the 21-cm global signal to Pop III stars and their remnants in faint galaxies.

The signal models described in this section are used to create the signal training set, an essential component of our observational strategy from which the signal extraction pipeline calculates the main modes of variation of the signal. The new data expected from JWST and from CMB missions will constrain parameter space, which will allow us to restrict the training set and reduce parameter degeneracies and covariances. See Section 6 for more details on the training set and its effect on the uncertainty of our signal estimate.

4. FOREGROUNDS

Here, we discuss the origin and properties of the foregrounds expected in the 21-cm measurement from lunar orbit, which are modeled and accounted for in our signal extraction pipeline.

4.1. Galaxy/Extragalactic Foregrounds

Beam-averaged diffuse sky foregrounds represent the strongest contributors to any highly redshifted 21-cm measurement for a space-based experiment. The most important arises from our Galaxy (Shaver et al. 1999). In addition, a “sea” of Extragalactic sources appear as another diffuse, spectrally-featureless power-law foreground (at DARE’s resolution) and contributes $\sim 10\%$ of the total sky brightness temperature (Figure 2). The emission from these foregrounds is produced by synchrotron radiation that intrinsically has a smooth frequency spectrum (e.g., Bernardi et al. 2015; Petrovic & Oh 2011). On top of the spectral smoothness, the foregrounds are spatially variable (inset in Figure 2). Their featureless spectrum and spatial variability contrast with the spectral features and spatial uniformity of the 21-cm spectrum, making them separable (Liu et al. 2013; Switzer & Liu 2014).

Theoretical models predict that the foreground is well approximated by a third-order polynomial to levels below the amplitude of the 21-cm global signal, especially over low-foreground regions (Bernardi et al. 2015). Smoothness over a frequency range much broader than ~ 40 -120 MHz is supported by sky models produced from measure-

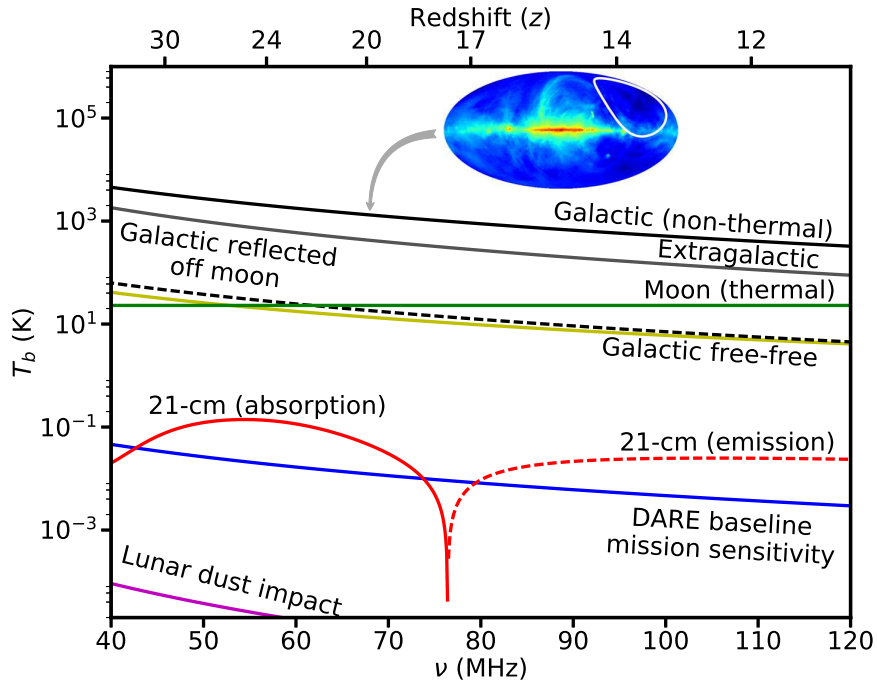


Figure 2. The Galactic and Extragalactic spectra for a typical region away from the Galactic center. The Galaxy spectrum also reflects off the Moon (Evans 1969). The Moon’s thermal emission at low radio frequencies arises from cold, uniform subsurface layers. The effects of hyperkinetic dust impacts on the spacecraft in orbit of the Moon are unimportant. The red curve illustrates the spectral features in the 21-cm spectrum, where the dashed part of the curve corresponds to emission and the solid to absorption for this log-linear plot. *Inset:* A Mollweide projection of the sky at 408 MHz (Haslam et al. 1982) along with a DARE beam FWHM white contour.

ments that cover the range 10 MHz - 5 THz (de Oliveira-Costa et al. 2008; Zheng et al. 2017; Sathyanarayana Rao et al. 2017). These models rely on, at most, five components to describe the spectral content of the foreground over several decades in frequency. Global measurements from the Experiment to Detect the Global EoR Signature (EDGES), Sonda Cosmológica de las Islas para la Detección de Hidrógeno Neutro (SCI-HI), Shaped Antenna measurement of the background RAdio Spectrum (SARAS), and Large-Aperture Experiment to Detect the Dark Ages (LEDA) provide further validation of the intrinsic foreground smoothness (Rogers & Bowman 2008; Mozdzen et al. 2017; Voytek et al. 2014; Patra et al. 2015; Bernardi et al. 2016).

In our strategy, we use a diffuse foreground model produced from all-sky observations taken at two frequencies, 45 and 408 MHz (Haslam et al. 1982; Guzmán et al. 2011), in order to account for spatial variations in the spectral index.

The spectrally smooth foreground is altered via the frequency-dependent antenna response (Vedantham et al. 2014; Bernardi et al. 2015; Mozdzen et al. 2016). The beam directivity of finite-sized, wideband antennas does not remain constant across frequency (Rumsey 1966). This beam “chromaticity” impacts the observed spectrum of the spatially-dependent foregrounds. The variation with frequency of the beam shape and directivity imprints spectral structure into the beam-averaged response that is not intrinsic to the foregrounds.

As part of our strategy, chromaticity is addressed by minimizing instrumental design effects and making precise beam measurements on the ground and on-orbit. We

also estimate the beam chromaticity by modulating the beam-averaged foregrounds through rotation of the antenna about the boresight axis. This technique is discussed in Section 5. This represents a significant advancement over previous simulations. For instance, in Harker et al. (2016), the beam was taken to be Gaussian and the integrated foreground was assumed to perfectly follow a polynomial of the form $\ln(T) = \sum_{i=0}^5 a_i \ln(\nu)^i$.

Finally, we note that the low foreground areas of the sky are polarized to a few percent ($\lesssim 5\%$) (Jelić et al. 2014, 2015; Lenc et al. 2016). Our dual polarization instrument directly measures this intrinsic sky polarization. At the same time, this polarization is minimized through dilution produced by our wide antenna beam, and also averaged down by our scanning strategy, which includes antenna rotation.

4.2. Other Foregrounds

21-cm cosmology experiments in lunar orbit will also detect emission from the Moon via the antenna back-lobe. The lunar spectrum is comprised of (1) thermal emission from a ~ 100 m subsurface layer (i.e., electrical skin depth of the regolith) (Salisbury & Fernald 1971; Keihm & Langseth 1975) and (2) reflected Galactic emission, requiring a parameter in the data analysis pipeline to describe the Moon’s reflectivity (Davis & Rohlfs 1964; Vedantham et al. 2015).

Other processes have a minor effect on the spectrum. Hyperkinetic impacts of dust from the interplanetary medium and the lunar exosphere on the spacecraft surface generate radio transients (e.g., Meyer-Vernet 1985); but the dust distribution around the Moon (e.g., Stubbs

et al. 2010), the capacitance of the spacecraft, and solar wind conditions produce most of its emission at frequencies < 40 MHz (Figure 2; Le Chat et al. 2013).

Bright, transient, nonthermal emission from Jupiter and Io also occur at < 40 MHz (Panchenko et al. 2013; Cecconi et al. 2012); however, at 40-120 MHz, the antenna temperature observed by an instrument like that proposed for DARE is only ~ 1 mK for Jupiter (Zarka 2004). Jupiter, and other astronomical sources such as Cas A (similarly beam-diluted), may introduce low-level spectral effects due to scattering off the spacecraft. Electromagnetic analysis, incorporating accurate models of the spacecraft, must be used to assess and calibrate these effects as part of the signal extraction pipeline.

Finally, atoms (e.g., carbon) in cold, diffuse gas in the Milky Way (and possibly in the IGM) produce radio recombination lines (RRLs; Peters et al. 2011; Morabito et al. 2014). These lines are sharp (~ 10 kHz wide), but spaced at known intervals of ~ 1 MHz. Spectral channels containing RRLs constitute a negligible fraction of the data and may be discarded. Removal of potential RRLs from the 21-cm spectrum will drive the spectral resolution of the science instrument. Also, beam dilution is expected to significantly reduce any impact from recombination lines.

5. THE DARE SCIENCE INSTRUMENT

To illustrate how the cosmological 21-cm spectrum can be extracted from the foregrounds, we use the new science instrument proposed for DARE (Figure 3). In Burns et al. (2012), we outlined a very basic approach for idealized, lunar-based 21-cm cosmology observations. We have now advanced the fidelity of the instrument model to evaluate measurements of the spectrum and constrain parameters for the first luminous objects at the significance level presented in Section 2, in the presence of realistic and well modeled uncertainties.

Figure 4 shows a block diagram of the current DARE instrument design, which consists of four subsystems: (1) an antenna composed of a pair of crossed biconical dipoles above a ground plane that provides dual polarization with low reflection coefficient (-12 dB average across the band) and beam chromaticity (the beam directivity spectral knowledge goal is ~ 20 ppm, see below); (2) a thermally-controlled receiver with a calibration architecture that utilizes precise continuous-wave frequency tones optimized to yield a frequency response that meets DARE’s RMS criterion; (3) a spectrometer with a wide bandwidth and digital receiver that provides the spectral resolution and Stokes processing of the V and H channels; and (4) an instrument electronics subsystem to interface with the spacecraft. The expectation for the instrument envelopes the hardware performance of systems on the ground (e.g., EDGES, Bowman & Rogers 2010; Cosmic Twilight Polarimeter, CTP, Nhan et al. 2017) and in space (Global Precipitation Measurement Microwave Imager, GMI²).

We model the forward instrument response following that used by EDGES (Monsalve et al. 2017) as:

$$P = g [|F|^2 (\eta_l T_A + (1 - \eta_l) T_{Ap}) (1 - |\Gamma_A|^2) + T_{off}] , \quad (2)$$

where P is the raw power measured by the instrument, g and T_{off} represent the system gain and radiometric offset respectively, η_l accounts for the antenna and balun losses at physical temperature T_{Ap} , $1 - |\Gamma_A|^2$ accounts for the reflection coefficient of the antenna, and $|F|^2$ is the throughput of the receiver front end accounting for multiple reflections between the receiver and antenna. The instrument calibration activities consist of using ground, on-board and on-orbit calibration to invert the forward instrument response model and provide an estimate of the antenna temperature T_A .

During science observations, the receiver is calibrated continuously using the pilot tone injection receiver architecture. The calibration system generates tones at ≈ 5 frequencies simultaneously across the band to adequately sample the frequency range. The tones are each within a single 50 kHz spectrometer bin, and thus produce negligible degradation in spectral performance. The nominal calibration cycle consists of a sequence of four states which are enabled for 10 seconds each: 1) high-level tones directed toward the receiver, 2) low-level tones directed toward the receiver, 3) high-level tones directed toward the antenna, and 4) low-level tones directed toward the antenna. The gain of the receiver is computed by differencing instrument-measured power from the high- and low-level injected tones toward the receiver divided by the difference in effective input brightness temperature of the tones characterized during pre-flight calibration. Likewise, the tones injected toward the antenna afford an on-board measurement of the antenna reflection computed in a similar fashion.

The terms T_{off} , η_l , and $|F|^2$ in Equation 2 are computed based on ground measurements and the on-orbit trending of the receiver gain and reflection coefficient.

The DARE antenna and receiver are designed to minimize temperature variations by limiting exposure to the solar flux and lunar albedo. For the antenna, thermal baffles, as shown in Figure 3, result in a predicted physical temperature change over the lunar orbit of 10°C allowing DARE to maintain a nearly constant beam directivity. The front-end receiver includes a proportional-integral-derivative temperature control to provide predicted thermal stability of 0.1°C , thus reducing receiver systematics to meet DARE’s calibration and stability requirements.

A novel feature of the current design is on-orbit calibration of the antenna directivity. Measurements of the beam will be obtained by receiving ≥ 3 narrow-band, circularly-polarized signals spaced across the band, transmitted from a large antenna on the Earth as DARE orbits the Moon above the nearside. The spacecraft (and antenna) is slowly rotated while it continuously receives these signals. The received signal power at each frequency as a function of antenna pointing will produce a slice through the beam power pattern. The transmitted signals will also reflect off the lunar regolith and return to the same antenna on Earth to correct for ionospheric effects. The in-situ beam measurement system is currently being baselined to use the 140-foot radio telescope at the Green Bank Observatory, operating with 50% aperture

² <https://pmm.nasa.gov/gpm/flight-project/gmi>

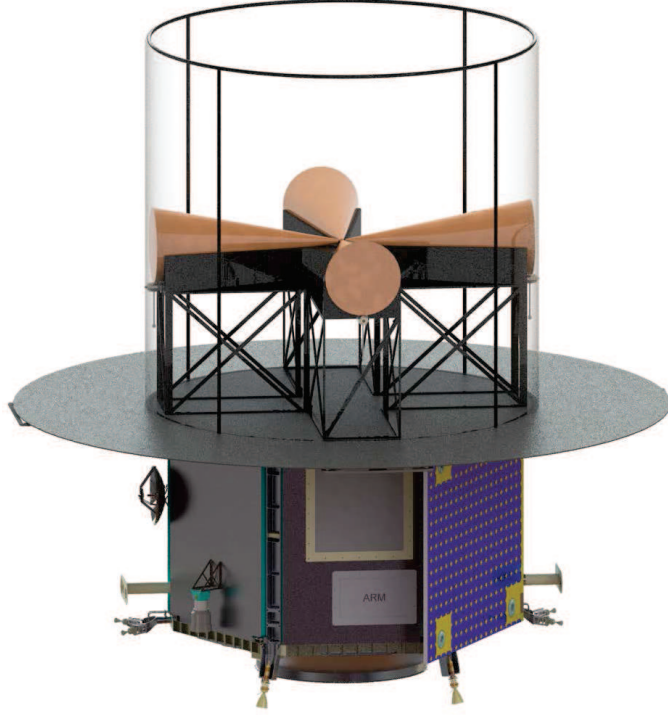


Figure 3. An artistic rendering of the DARE observatory. The science instrument thermal shield surrounds the antenna (shown transparent for clarity). The antenna consists of a pair of dual, crossed bicones. Beneath the antenna support structure is a deployed ground plane which aids in shaping the beam directivity. Below the instrument is the spacecraft bus including the solar panels and telemetry system.

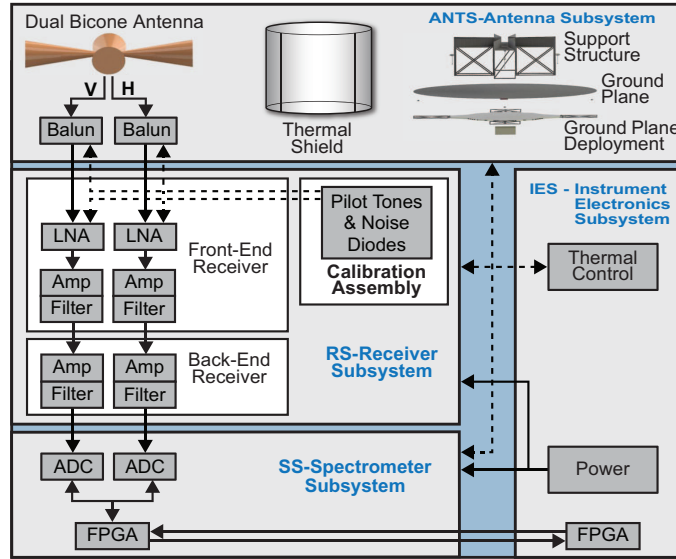


Figure 4. DARE instrument block diagram. DARE consists of four subsystems: dual polarization antenna, pilot tone calibration receiver, high resolution digital spectrometer, and a standard instrument electronics module for power, data handling, and instrument control that interfaces with the spacecraft.

efficiency, transmitting 10 kW of power, and using 10 second averaging.

Another innovation in the current design of DARE is polarization measurements to constrain and distinguish the beam-averaged foregrounds from the unpolarized HI signal (Nhan et al. 2017). Our observation strategy incorporates rotation of the antenna about the boresight axis to modulate the signals captured by the two polar-

ization arms of the antenna. This modulation results in induced polarization that tracks and measures the beam-averaged foreground spectrum, without relying on e.g., polynomial model fits, and is insensitive to the spatially uniform 21-cm signal. CMB polarization measurements use analogous modulation approaches, achieving stability and systematic control required for μK polarimetric sensitivity (e.g., Bennett et al. 2003; Bischoff et al. 2013).

The on-orbit measurements of the antenna directivity and the induced polarization technique enable us to anticipate a knowledge of the beam-averaged foregrounds at a level of ~ 20 ppm. This represents an important advancement that allows us to achieve our goal of < 20 mK RMS spectral uncertainty on the extracted 21-cm models.

6. EXTRACTING THE COSMIC 21-CM SPECTRUM

In this section we demonstrate an essential aspect of our observational strategy: how our data analysis pipeline is able to separate the 21-cm signal from foregrounds measured through a realizable instrument. We model each of these components, signal along with the foreground and instrument systematics, as described below.

In our previous work (Harker et al. 2012, 2016 hereafter H12 and H16), we developed a foundation for a 21-cm signal extraction pipeline using a Markov Chain Monte Carlo (MCMC) framework. However, we assumed an idealized instrument with exact knowledge of most instrument systematics and the form of the beam-averaged foreground. We have now significantly expanded the initial analyses of H12 and H16 by implementing a robust SVD modeling scheme based upon a pragmatic end-to-end instrument model (Section 5). Specifically, the current pipeline (which will be released to the community in a later publication) incorporates the following aspects for the first time:

- Full simulations of the antenna beam-weighted foreground. These simulations are based upon beam patterns calculated by the CST electromagnetic simulation package³ and our diffuse foreground model, described in Section 4.
- A calibration model, based upon expected lab measurements and uncertainties, that includes all parameters in Equation 2. The instrument model described in H12 included only the antenna reflection coefficient.
- A modeling scheme, detailed below, based upon the implementation of SVD on well-characterized training sets for both the signal and a complete set of instrument and foreground systematics. The SVD technique independently determines the main modes of variation in the signal and systematics. The MCMC algorithm then simultaneously fits all the coefficients associated with the SVD modes to extract the signal. This is a major improvement over our previous use of polynomials (Fourier series) to fit the foreground (reflection coefficient).

The MCMC algorithm in the pipeline samples the likelihood function

$$\ln L(\gamma) = -\frac{1}{2} \sum_{r=1}^{N_r} \sum_{i=1}^{N_\nu} \left[\frac{T_{A,D}^{(r)}(\nu_i) - T_{A,M}^{(r)}(\nu_i, \gamma)}{\sigma_r(\nu_i)} \right]^2, \quad (3)$$

where $T_{A,D}^{(r)}(\nu)$ and $T_{A,M}^{(r)}(\nu)$ are the antenna temperature spectra for the data (D) and the model (M), r and

ν indicate the sky direction and frequency channel, respectively, and $\sigma_r(\nu) = T_{A,D}^{(r)}(\nu)/\sqrt{\Delta\nu\Delta t}$ is the thermal noise level in the data for a given frequency bin of width $\Delta\nu$ centered on ν integrated over a time Δt .

We model $T_{A,M}^{(r)}(\nu)$ as a linear combination of (dimensionless) principal modes derived from SVD analyses (Switzer & Liu 2014; Paciga et al. 2013; Vedantham et al. 2014),

$$T_{A,M}^{(r)}(\nu, \gamma) = \sum_{i=1}^n (\gamma_{21})_i f_i(\nu) + \sum_{j=1}^m (\gamma_{sys})_j^{(r)} g_j(\nu), \quad (4)$$

where $f_i(\nu)$ and $g_j(\nu)$ are the SVD signal and systematic modes, respectively, and $(\gamma_{21})_i$ and $(\gamma_{sys})_j$ (both with units K) are the coefficients associated with each of them. We fit the entire parameter space, $\gamma = [\gamma_{21}, \gamma_{sys}]$, simultaneously (using the EMCEE code; Foreman-Mackey et al. 2013) in order to account for the covariance between all parameters and ensure self-consistency. This MCMC calculation efficiently and robustly obtains the full posterior distribution.

In this work, we utilize $n = 6$ (signal) and $m = 7$ (systematic) SVD modes because they are able to fit our fiducial models to within the thermal noise level achieved through 800 hours of integration. For future analyses, however, we are developing a novel technique that will choose the optimal number of modes to use in the pipeline. The details of this key advancement will be described in forthcoming works (Tauscher et al., in prep.; Rapetti et al., in prep.).

The systematic modes $g_j(\nu)$ are derived from 10,000 simulated datasets which vary the foreground and instrument within expected uncertainties. This process utilizes Equation 2, its inverse, and the fiducial values of the calibration and beam-weighted foreground parameters (Tauscher et al. in prep.). Currently, the signal modes $f_i(\nu)$ are derived from input training sets of 21-cm spectrum simulations (15,000 and 960, respectively) based on two well-motivated ranges of physical models (primordial Pop II and Pop III stars; see Section 3).⁴ In future work, the signal models will be combined into a single training set.

The Bayesian nature of the MCMC permits the incorporation of key prior knowledge on the instrument calibration and foregrounds when retrieving the posterior probability distribution of the model parameters. In the instrument simulations, we account for all the identified uncertainties and priors, including a 50 mK constraint on the beam-averaged foregrounds from measurements of the induced polarization. Even though, at this stage, the induced polarization is used only as a prior on the antenna temperature, T_A , in future work, all four Stokes parameters will be included in the likelihood function.

Figure 5 shows the SVD modes used in this work. The left and middle panels contain the signal modes for the models of primordial Pop II and Pop III stars, respectively. For the purpose of reducing the covariance be-

⁴ Each set of simulations was derived by randomly sampling the parameter space surveyed in Mirocha et al. (2017), with the addition of two parameters that describe the UV and X-ray photon production efficiency in minihalos (i.e., those with $T_{\text{virial}} < 10^4$ K). The Pop III models include only those with Region D extrema in emission.

³ <https://www.cst.com/>

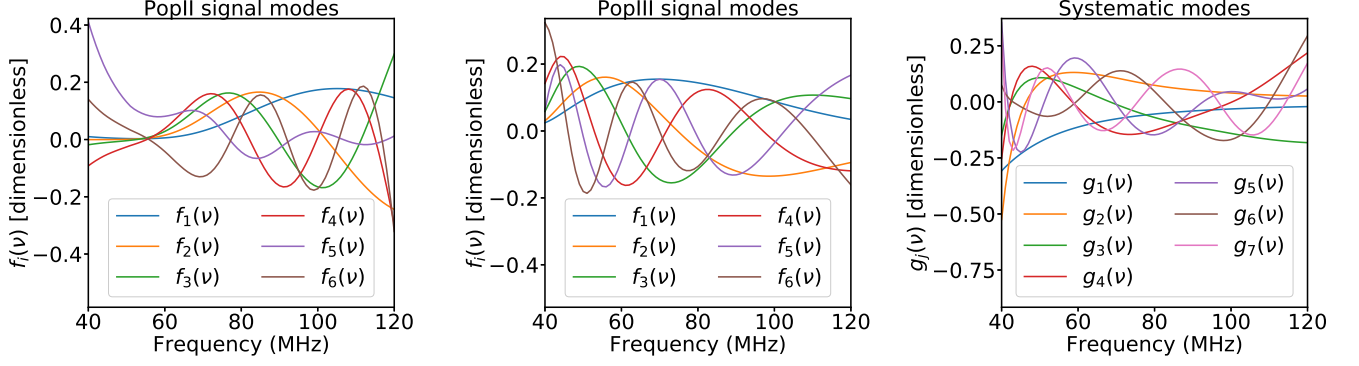


Figure 5. Left panel: the 6 principal SVD signal modes derived from 21-cm spectrum simulations of models based on primordial Pop II stars. Middle panel: the same but for signal models based on primordial Pop III stars. Right panel: the 7 principal SVD systematic modes derived from simulations of the instrument plus foreground. Each panel contains a set of orthonormal models, i.e. the curves represent only dimensionless shapes which are then multiplied by coefficients with units of temperature (K). The ability to separate the 21-cm signal from DARE’s systematics hinges on the ability to distinguish between the signal modes, $f_i(\nu)$, and the systematic modes, $g_j(\nu)$.

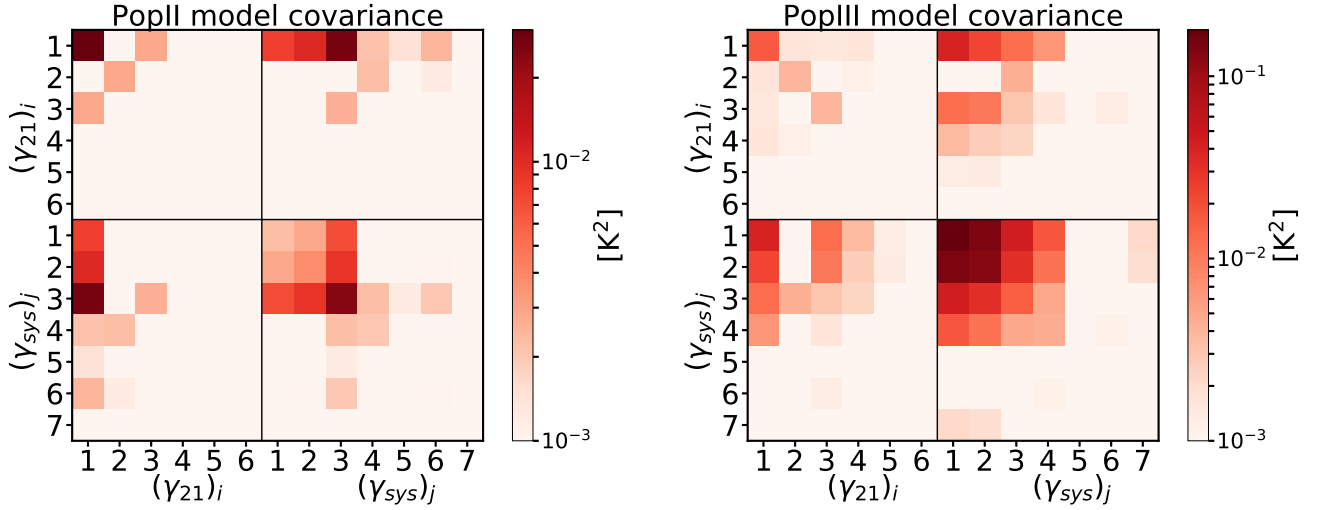


Figure 6. Covariance matrices for the 6 SVD signal parameters, $(\gamma_{21})_i$ for $i \in \{1, 2, \dots, 6\}$, and the 7 SVD systematic parameters, $(\gamma_{sys})_j$ for $j \in \{1, 2, \dots, 7\}$, used for fitting the primordial Pop II (left panel) and Pop III (right panel) stellar models. For ease of viewing, the absolute values of the covariances are shown. The vertical and horizontal black lines separate the regions with covariances between signal parameters (top left) and systematic parameters (bottom right). The other two regions are symmetric and show the covariances between parameters multiplying signal and systematic modes.

tween our parameters, γ , it is important that the SVD systematic modes are as orthogonal as possible (i.e. have a minimal dot product) with the SVD signal modes. When comparing one signal mode with the systematic mode of the same order (color) in Figure 5, we note that the shapes of the modes are sufficiently different to enable a clean extraction of the signal (see Figure 7).

Figure 6 shows the covariance matrix of the 6 signal parameters, $(\gamma_{21})_i$ with $i \in \{1, 2, \dots, 6\}$, and the 7 systematic parameters, $(\gamma_{sys})_j$ with $j \in \{1, 2, \dots, 7\}$. The top left corners within each of the 4 regions in both panels of Figure 6 demonstrate that the lowest order signal modes have enough similarities in shape with the first 3-4 systematic modes to generate only modest covariances.

By simultaneously fitting all parameters, γ , and marginalizing over the systematic parameters, γ_{sys} , we are able to clearly separate the signal from the systematics despite those covariances, as shown in Figure 7. The widths of the uncertainty bands result from the covari-

ances between the signal parameters, which depend on the level of overlap between the signal and systematic modes. This will be explored in detail in upcoming work (Tauscher et al., in prep.).

In summary, for the DARE instrument parameters discussed in Section 5 and 800 hours of total integration above the lunar farside, our signal extraction pipeline recovers the spectra and uncertainties for two representative models (Pop II and Pop III star models) shown in Figure 7. In addition to the 21-cm signal, the pipeline simultaneously fits the SVD modes of the receiver, beam, and foreground utilizing prior information and on-orbit measurements. With an average RMS of ≈ 17 mK, we recover the major features in the spectra and differentiate between different stellar population models.

7. PHYSICAL PARAMETER ESTIMATION

With the calibrated spectra and uncertainties in Figure 7, it is straight-forward to estimate when the first lumi-

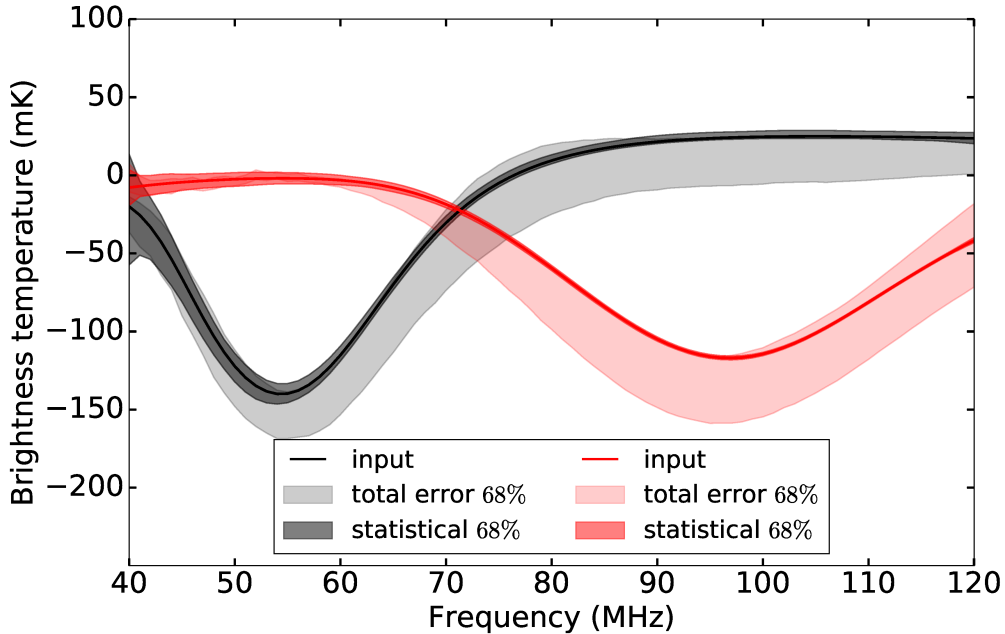


Figure 7. The extracted 21-cm spectra with 68% confidence intervals for models with primordial Pop II (red) and Pop III (black) stars expected using the DARE instrument parameters and 800 hours of observation. The dark bands represent thermal (statistical) noise from the sky. The total uncertainty, including statistical plus systematic effects from the instrument and foreground, is shown by the lighter bands, which are dominated by the covariance between the SVD signal and systematic modes.

nous objects ignited and began reionizing the Universe. Since redshift maps directly to frequency, measurements of the extrema frequencies from the 21-cm spectrum determine when major events occurred in a mostly model-independent fashion (Harker et al. 2016). The frequency of the Region B extremum (ν_B) determines the z at which the UV background activates the 21-cm transition (i.e., first stars ignition). This clean and accurate measurement delineates the nature of the first stars, especially considering that no observational bounds currently exist. Using a Pop III model as a working example, DARE will extract ν_B with a 1% (0.4 MHz) uncertainty (68% confidence). Similarly, the redshift when the first black holes began accretion is measured from the Region C extremum frequency (ν_C) with 1% (0.6 MHz) uncertainty. The redshift of the beginning of reionization is measured from the extremum ν_D with 2% (2 MHz) uncertainty. Different models (Figure 1) yield similar uncertainties for the extrema frequencies.⁵

The characteristics of the first stars and galaxies, along with the history of the early Universe, are determined from modeling of the calibrated spectrum. First, the history of reionization in the early Universe is characterized by the HI fraction (x_{HI}) and the IGM kinetic temperature (T_K) at $z \sim 11$. Our modeling of features in Region D using DARE’s sensitivity yields uncertainties of 5% and 10% for x_{HI} and T_K , respectively.

Next, the features in the 21-cm spectrum at the lowest frequencies depend upon the stellar populations that

dominate the UV background; if, for example, Pop III star formation is efficient, we should expect features of the signal to occur at lower frequencies (higher redshift) than if Pop II stars dominate the background because Pop II stars form in more massive halos which do not become abundant until relatively late times (low redshift). DARE’s sensitivity can separate the effects of the broad classes of Pop II and Pop III stellar models considered in this work (see Figures 1 and 7), subject to the assumed calibration of the Pop II contribution (see Section 3; Mirocha et al. 2017) and the model for Pop III stars. A useful metric for gauging the influence of Pop III is the ratio of UV production efficiencies for Pop III compared to Pop II stars, $\xi_\alpha \equiv \xi_{\alpha,III}/\xi_{\alpha,II}$. The value of $\xi_{\alpha,II}$ is drawn from the BPASS models (Eldridge & Stanway 2009) assuming solar metallicity, while $\xi_{\alpha,III}$ is allowed to vary freely. DARE constrains $\xi_{\alpha,III}$ with 25% uncertainty in Figure 8.

The characteristics of the first X-ray sources (Region C in Figure 1) are inferred from the ratio of X-ray heating efficiencies between Pop III and Pop II stars. Analogous to the UV constraints, the Pop III X-ray efficiency, $\xi_{X,III}$, is allowed to vary freely, while $\xi_{X,II}$ is anchored to the local relation between X-ray luminosity and SFR (Mineo et al. 2012a) assuming high-mass X-ray binaries are the dominant source. DARE can measure $\xi_{X,III}$ with 15% uncertainty (see Figure 8). Further modeling plus multi-wavelength observations (e.g., the cosmic X-ray background; Fialkov et al. 2017) may help to better constrain the identity of the Universe’s first X-ray sources, whether they be black hole X-ray binaries, hot gas in star-forming galaxies, or proto-quasars.

Finally, before concluding, we emphasize that these Pop III models are quite simple, as, for example, they ne-

⁵ Note that the extrema locations are determined from the full signal model on each step of the MCMC, i.e., these quantities have not assumed a cubic spline form for the signal as in some previous works (Harker et al. 2012).

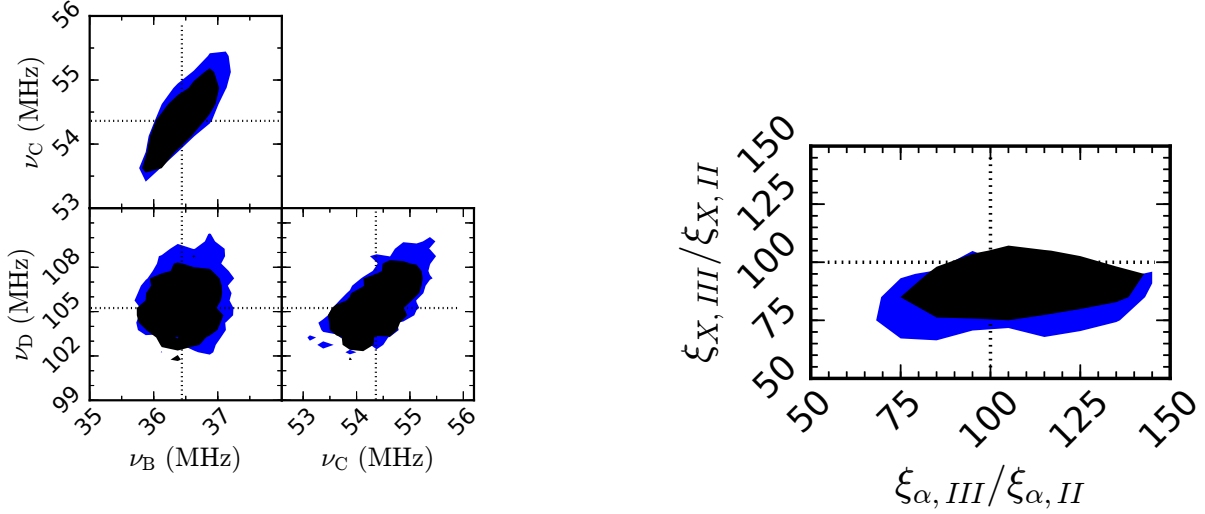


Figure 8. The panels illustrate examples of constraints on the global 21-cm extrema frequencies (left), UV photon production efficiency (ξ_α) and X-ray heating efficiency (ξ_X) between models with Pop III and Pop II stars (right) using the calibrated 21-cm spectrum. Dotted black lines indicate the “true” input values. The contours are at the 68% confidence intervals using 23 (black) and 30 (blue) mK average RMS uncertainties over the observed band.

glect an explicit treatment of feedback. As a result, the interpretation of the precise value of $\xi_{\alpha,III}/\xi_{\alpha,II}$ may be considerably more complex in practice, but the finding that both values are non-zero is robust.

8. CONCLUDING REMARKS

To achieve the science potential of 21-cm global spectral observations, we proposed an observational strategy that carefully considers the local environment, the instrument, and the methods for signal extraction. A lunar-orbiting experiment above the Moon’s farside has the best probability of measuring the 21-cm spectrum since this environ is free of ionospheric effects and human-generated radio frequency interference.

Signal extraction in the presence of bright foregrounds is the greatest challenge for all observations of the 21-cm cosmological spectrum. Utilizing Singular Value Decomposition to model the foreground and instrument along with a Markov Chain Monte Carlo numerical inference technique to survey parameter space, we showed that it is possible to accurately recover the expected features in the spectrum in the presence of bright foregrounds with the instrument characteristics of the *Dark Ages Radio Explorer* (DARE) for ≈ 800 hrs of integration. To separate the signal from the foreground, the antenna system must be well-characterized requiring temperature control and precise beam directivity measurements on the ground and in-space. In addition, a model-independent constraint on the foreground from polarimetric observations is an important element in the signal extraction.

From the extracted 21-cm spectrum (including confidence intervals), we showed that meaningful constraints can be placed upon the physical parameters of primordial radiating objects. The redshift for the commencement of first star formation and X-ray emission from the first

accreting black holes along with the redshift of the beginning of reionization can be inferred to within \approx a few percent. The 21-cm signal is also uniquely sensitive to the different radiation effects produced by Pop II and Pop III stellar models. Specifically, the UV production and X-ray heating efficiencies can be constrained, thus determining which stellar population was dominant within the first galaxies. Finally, the history of reionization in the early Universe can be characterized by the redshift evolution of the HI ionization fraction (x_{HI}) inferred from the 21-cm spectrum.

Accurate parameter estimation is a core capability required for 21-cm global signal observations and interpretations. Bayesian methods have significant potential for 21-cm observations (Greig et al. 2016; Bernardi et al. 2016). They have proven to be successful for other experiments targeting weak signals, including CMB observations (Planck Collaboration et al. 2016a,b) and the LIGO gravitational wave detections (Abbott et al. 2016; Veitch et al. 2015). The next step in the analyses of the global 21-cm spectrum is to construct a likelihood function allowing differentiation between differing physical models for the first halos. Similarly, modeling different levels of structure in the beam-convolved foregrounds needs a refined Bayesian approach. This is a highly computationally intensive process. We are refining and extending our SVD modeling approach towards these goals. In addition, recent developments of Nested Sampling algorithms for high dimensional parameter spaces which operate in massively parallel computer architectures (Handley et al. 2015) have great potential for 21-cm cosmology applications.

In conclusion, measurements of spectral features in the 21-cm spectrum will answer key science questions from the NRC Astrophysics Decadal Survey: “What were the

first objects to light up the Universe and when did they do it?” With a clean measurement within the radio-quiet environs of the Moon’s farside and proven technology, the 21-cm global signal will open a new window of discovery into the early Universe.

This research was supported by the NASA Ames Research Center via grants NNA09DB30A, NNX15AD20A, NNX16AF59G, as well as by a NASA SSERVI Cooperative Agreement to JB. The theoretical work was partially funded by NASA ATP grant NNX15AK80G to SF and JB. DR is supported by a NASA Postdoctoral Program Senior Fellowship at the NASA Ames Research Center, administered by the Universities Space Research Association under contract with NASA. We thank the following colleagues for their important contributions including Jill Bauman, Jay Bookbinder, Matthew D’Ortenzio, Robert Hanel, Butler Hine, Joseph Lazio, Stephanie Morse, Ken Galal, Laura Plice, Gary Rait, Jeremy Stober, and Eugene Tu. We also benefited from helpful input from James Aguirre, Mina Cappuccio, James Condon, Steven Ellingson, Bryna Hazelton, Danny Jacobs, Mark LaPole, Adam Lidz, John Mather, Harry Partridge, Aaron Parsons, Jonathan Pober, Greg Schmidt, Greg Taylor, and Sandy Weinreb.

REFERENCES

- Abbott, B. P., Abbott, R., Abbott, T. D., et al. 2016, *Physical Review Letters*, 116, 061102
- Alexander, J. K., & Kaiser, M. L. 1976, *J. Geophys. Res.*, 81, 5948
- Barkana, R., & Loeb, A. 2005, *ApJ*, 624, L65
- Bennett, C. L., Bay, M., Halpern, M., et al. 2003, *ApJ*, 583, 1
- Bernardi, G., McQuinn, M., & Greenhill, L. J. 2015, *ApJ*, 799, 90
- Bernardi, G., Zwart, J. T. L., Price, D., et al. 2016, *MNRAS*, 461, 2847
- Bharadwaj, S., & Ali, S. S. 2004, *MNRAS*, 352, 142
- Bischoff, C., Brizius, A., Buder, I., et al. 2013, *ApJ*, 768, 9
- Bittner, J. M., & Loeb, A. 2011, *J. Cosmology Astropart. Phys.*, 4, 38
- Bowman, J. D., & Rogers, A. E. E. 2010, *Nature*, 468, 796
- Brorby, M., Kaaret, P., Prestwich, A., & Mirabel, I. F. 2016, *MNRAS*, 457, 4081
- Burns, J. O., Lazio, J., Bale, S., et al. 2012, *Advances in Space Research*, 49, 433
- Cecconi, B., Hess, S., Hérique, A., et al. 2012, *Planet. Space Sci.*, 61, 32
- Datta, A., Bradley, R., Burns, J. O., et al. 2016, *ApJ*, 831, 6
- Davies, K. 1990, in *International Beacon Satellite Symposium 1990*, ed. J. R. Manzano, 153–157
- Davis, J. R., & Rohlf, D. C. 1964, *J. Geophys. Res.*, 69, 3257
- de Oliveira-Costa, A., Tegmark, M., Gaensler, B. M., et al. 2008, *MNRAS*, 388, 247
- Eldridge, J. J., & Stanway, E. R. 2009, *MNRAS*, 400, 1019
- Evans, J. V. 1969, *ARA&A*, 7, 201
- Ewen, H. I., & Purcell, E. M. 1951, *Nature*, 168, 356
- Fialkov, A., Cohen, A., Barkana, R., & Silk, J. 2017, *MNRAS*, 464, 3498
- Field, G. B. 1958, *Proceedings of the IRE*, 46, 240
- Foreman-Mackey, D., Hogg, D. W., Lang, D., & Goodman, J. 2013, *PASP*, 125, 306
- Furlanetto, S. R. 2006, *MNRAS*, 371, 867
- Furlanetto, S. R., & Johnson Stoefer, S. 2010, *MNRAS*, 404, 1869
- Furlanetto, S. R., Oh, S. P., & Briggs, F. H. 2006, *Phys. Rep.*, 433, 181
- Greig, B., Mesinger, A., & Pober, J. C. 2016, *MNRAS*, 455, 4295
- Guzmán, A. E., May, J., Alvarez, H., & Maeda, K. 2011, *A&A*, 525, A138
- Handley, W. J., Hobson, M. P., & Lasenby, A. N. 2015, *MNRAS*, 450, L61
- Harker, G. J. A., Mirocha, J., Burns, J. O., & Pritchard, J. R. 2016, *MNRAS*, 455, 3829
- Harker, G. J. A., Pritchard, J. R., Burns, J. O., & Bowman, J. D. 2012, *MNRAS*, 419, 1070
- Haslam, C. G. T., Salter, C. J., Stoffel, H., & Wilson, W. E. 1982, *A&AS*, 47, 1
- Jelić, V., de Bruyn, A. G., Mevius, M., et al. 2014, *A&A*, 568, A101
- Jelić, V., de Bruyn, A. G., Pandey, V. N., et al. 2015, *A&A*, 583, A137
- Keihm, S. J., & Langseth, M. G. 1975, *Icarus*, 24, 211
- Le Chat, G., Zaslavsky, A., Meyer-Vernet, N., et al. 2013, *Sol. Phys.*, 286, 549
- Lenc, E., Gaensler, B. M., Sun, X. H., et al. 2016, *ApJ*, 830, 38
- Liu, A., Pritchard, J. R., Tegmark, M., & Loeb, A. 2013, *Phys. Rev. D*, 87, 043002
- Liu, L., Le, H., Chen, Y., et al. 2011, *Journal of Geophysical Research (Space Physics)*, 116, A09307
- Loeb, A., & Furlanetto, S. R. 2013, *The First Galaxies in the Universe*, ISBN: 9780691144917, Princeton, NJ: Princeton University Press.
- Madau, P., Meiksin, A., & Rees, M. J. 1997a, *ApJ*, 475, 429
- , 1997b, *ApJ*, 475, 429
- Mather, J., Hinshaw, G., & Page, L. 2013, *Cosmic Microwave Background in Planets, Stars and Stellar Systems. Volume 6: Extragalactic Astronomy and Cosmology*, ed. T. D. Oswalt & W. C. Keel, 609
- McKinley, B., Briggs, F., Kaplan, D. L., et al. 2013, *AJ*, 145, 23
- Mercier, C., & Trotter, G. 1997, *ApJ*, 474, L65
- Mesinger, A., Furlanetto, S., & Cen, R. 2011, *MNRAS*, 411, 955
- Meyer-Vernet, N. 1985, *Advances in Space Research*, 5, 37
- Mineo, S., Gilfanov, M., & Sunyaev, R. 2012a, *MNRAS*, 419, 2095
- , 2012b, *MNRAS*, 426, 1870
- Mirocha, J., Furlanetto, S. R., & Sun, G. 2017, *MNRAS*, 464, 1365
- Mirocha, J., Harker, G. J. A., & Burns, J. O. 2015, *ApJ*, 813, 11
- Monsalve, R. A., Rogers, A. E. E., Bowman, J. D., & Mozdzen, T. J. 2017, *ApJ*, 835, 49
- Morabito, L. K., Oonk, J. B. R., Salgado, F., et al. 2014, *ApJ*, 795, L33
- Morales, M. F., & Wyithe, J. S. B. 2010, *ARA&A*, 48, 127
- Mozdzen, T. J., Bowman, J. D., Monsalve, R. A., & Rogers, A. E. E. 2016, *MNRAS*, 455, 3890
- , 2017, *MNRAS*, 464, 4995
- Nhan, B. D., Bradley, R. F., & Burns, J. O. 2017, *ApJ*, 836, 90
- Paciga, G., Albert, J. G., Bandura, K., et al. 2013, *MNRAS*, 433, 639
- Panchenko, M., Rucker, H. O., & Farrell, W. M. 2013, *Planet. Space Sci.*, 77, 3
- Patra, N., Subrahmanyan, R., Raghunathan, A., & Udaya Shankar, N. 2013, *Experimental Astronomy*, 36, 319
- Patra, N., Subrahmanyan, R., Sethi, S., Udaya Shankar, N., & Raghunathan, A. 2015, *ApJ*, 801, 138
- Peters, W. M., Lazio, T. J. W., Clarke, T. E., Erickson, W. C., & Kassim, N. E. 2011, *A&A*, 525, A128
- Petrovic, N., & Oh, S. P. 2011, *MNRAS*, 413, 2103
- Planck Collaboration, Ade, P. A. R., Aghanim, N., et al. 2016a, *A&A*, 594, A13
- Planck Collaboration, Adam, R., Aghanim, N., et al. 2016b, *A&A*, 596, A108
- Plice, L., Galal, K., & Burns, J. O. 2017, *ArXiv e-prints*, arXiv:1702.00286
- Polygiannakis, J., Preka-Papadema, P., & Moussas, X. 2003, *MNRAS*, 343, 725
- Presley, M. E., Liu, A., & Parsons, A. R. 2015, *ApJ*, 809, 18
- Pritchard, J. R., & Loeb, A. 2010, *Phys. Rev. D*, 82, 023006
- , 2012, *Reports on Progress in Physics*, 75, 086901
- Rogers, A. E. E., & Bowman, J. D. 2008, *AJ*, 136, 641
- Rogers, A. E. E., Bowman, J. D., Vierinen, J., Monsalve, R., & Mozdzen, T. 2015, *Radio Science*, 50, 130
- Rumsey, V. 1966, *Frequency Independent Antennas*, Academic Press, Electronic Science Series, New York.
- Salisbury, W. W., & Fernald, D. L. 1971, *Journal of the Astronautical Sciences*, 18, 236
- Sathyanarayana Rao, M., Subrahmanyan, R., Udaya Shankar, N., & Chluba, J. 2017, *AJ*, 153, 26
- Shaver, P. A., Windhorst, R. A., Madau, P., & de Bruyn, A. G. 1999, *A&A*, 345, 380
- Shull, J. M., & van Steenberg, M. E. 1985, *ApJ*, 298, 268
- Singh, S., Subrahmanyan, R., Udaya Shankar, N., & Raghunathan, A. 2015, *ApJ*, 815, 88
- Sokolowski, M., Tremblay, S. E., Wayth, R. B., et al. 2015a, *PASA*, 32, 4
- Sokolowski, M., Wayth, R. B., Tremblay, S. E., et al. 2015b, *ApJ*, 813, 18
- Stubbs, T. J., Glenar, D. A., Colaprete, A., & Richard, D. T. 2010, *Planet. Space Sci.*, 58, 830
- Sun, G., & Furlanetto, S. R. 2016, *MNRAS*, 460, 417
- Switzer, E. R., & Liu, A. 2014, *ApJ*, 793, 102
- Vedantham, H. K., & Koopmans, L. V. E. 2015, *MNRAS*, 453, 925
- Vedantham, H. K., Koopmans, L. V. E., de Bruyn, A. G., et al. 2014, *MNRAS*, 437, 1056

- . 2015, MNRAS, 450, 2291
- Veitch, J., Raymond, V., Farr, B., et al. 2015, Phys. Rev. D, 91, 042003
- Voytek, T. C., Natarajan, A., Jáuregui García, J. M., Peterson, J. B., & López-Cruz, O. 2014, ApJ, 782, L9
- Wouthuysen, S. A. 1952, AJ, 57, 31
- Zarka, P. 2004, in Astronomical Society of the Pacific Conference Series, Vol. 321, Extrasolar Planets: Today and Tomorrow, ed. J. Beaulieu, A. Lecavelier Des Etangs, & C. Terquem, 160
- Zheng, H., Tegmark, M., Dillon, J. S., et al. 2017, MNRAS, 464, 3486